

Flux emergence event underneath a filament

J. Palacios¹, Y. Cerrato¹, C. Cid¹, A. Guerrero¹ and E. Saiz¹

¹Space Research Group–Space Weather, Departamento de Física y Matemáticas,
Universidad de Alcalá

University Campus, Sciences Building, P.O. 28871, Alcalá de Henares, Spain
email: judith.palacios@uah.es

Abstract. Flux emergence phenomena are relevant at different temporal and spatial scales. We have studied a flux emergence region underneath a filament. This filament elevated itself smoothly, and the associated CME reached the Earth. In this study we investigate the size and the amount of flux in the emergence event. The flux emergence site appeared just beneath a filament. The emergence acquired a size of 24 Mm in half a day. The unsigned magnetic flux density from LOS-magnetograms was around 1 kG at its maximum. The transverse field as well as the filament eruption were also analysed.

Keywords. Sun: photosphere, magnetic fields, filaments; techniques: polarimetric

1. Introduction

Flux emergence is one of the most important events in the solar photosphere, acting as part of the local dynamo or small-scale surface dynamo (e.g. Martínez Pillet, 2013). Sometimes the ubiquitous circumstance of flux emergence can be of such a large scale that it may affect structures in the chromosphere and the low corona. For an extensive review on the topic, see Cheung & Isobe (2014). The different spatial and temporal scales of flux emergence features have been reviewed by Schmieder *et al.* (2014).

The characteristics of emerging magnetic flux – basically its area and its magnetic flux density – and the total time employed by the feature to emerge, can be combined to get a temporal flux emergence growth rate for these events, as will be mentioned in the following paragraphs. Magnetic flux is measured in Weber (Wb), but Maxwell (Mx) is commonly used. The equivalence is 10^8 Mx to 1 Wb. Its temporal rate is given in Mx day^{-1} (or other unit of time) here.

Flux emergence episodes have been investigated in detail in the era of high-resolution spectropolarimetry. The largest cases, such as sunspot emergence, have been studied thoroughly, but smaller ones have remained evasive until recent times, due to the low spatial and spectral resolution of the observations. At the smallest scales, there are some studies at the granular level, such as De Pontieu (2002), and Orozco *et al.* (2008). Granular-scale simulations have also been performed, e.g., in Tortosa & Moreno-Insertis (2009). At the mesogranular scale, flux emergence cases found by Palacios *et al.* (2012) show growth rates of 10^{18} Mx in about 20 min. Spectral line inversions show field strengths of hectogauss in these mesogranular-sized patches (see Guglielmino *et al.* (2013). The flux emergence rates at these spatial scales from longitudinal synthetic magnetograms are in the same range, $\sim 10^{17}$ Mx min^{-1} (Cheung *et al.* 2008).

Some of these small emergence cases come in the form of loop-like features: two opposite polarities linked by a patch of transverse field. An amount of cases have been described in, e.g., Centeno *et al.* (2007), Gömöry *et al.* (2010), Palacios *et al.* (2012). Loop statistics, lifetimes and energy implications are described in Martínez González *et al.* (2009) and

Martínez González *et al.* (2010). In these very small emergence cases, the flux emergence rate is $\sim 10^{17}$ Mx min $^{-1}$.

We should also mention the ephemeral regions (EFR) which are manifestations of small bipolar emergence that constitute an important contribution to the solar surface magnetism. The typical flux emergence rate per feature is $\sim 10^{15}$ Mx s $^{-1}$, with total flux contents in the smaller EFRs of 10^{18} Mx. These features typically emerge over the course of several hours (Guglielmino *et al.* 2012), and contribute with 10^{22} Mx day $^{-1}$ to the total flux on the solar surface (Hagenaar, 2001). These regions are also taken into account for the calculation of the total solar irradiance, as shown in Krivova *et al.* (2007), among others. Other examples of small bipolar emergence fields are the serpentine fields – undulatory fields –, exhibiting U- and Ω -shaped loops. Vargas Domínguez *et al.* (2012) showed some observational examples. Valori *et al.* (2012) made force-free extrapolations of sea-serpent magnetic fields in the context of a large active region emergence.

Very recent large-scale flux emergence events have been investigated. Being intermediate to large sized active regions, the flux emergence growth rate may vary but it is around 10^{21} Mx day $^{-1}$ for active region emergence simulations, as in Rempel & Cheung (2014), and for observations, as in Centeno (2012). One of the largest simulated ARs can be found in Cheung *et al.* (2010), being almost an order of magnitude larger in flux emergence rate. Other interesting cases of active region emergence are the ‘anemones’ or fountain-like regions (Asai *et al.* 2008). These events are related to active regions growing into coronal holes, which consist of mostly open field lines extending into the interplanetary medium and acting as an ambient field that leads to reconnection.

Flux rope emergence is one of the occurrences with larger consequences for space-weather, since it may further trigger eruptions and CMEs in the aftermath. This emergence may be caused by the whole body emergence or further evolution of the magnetic field in an active region (see Cheung & Isobe 2014). Eventually it may provoke an eruption. These enormous eruptions may be caused by different physical mechanisms. Some of these processes do include flux emergence and cancellation by reconnection. For an exhaustive review, see e.g. Zuccarello *et al.* (2013). There are some reported cases of filament eruption and flux emergence (e.g. Wang & Sheeley 1999); still, the direct cause-effect relationship between flux emergence and filament eruption is not that clear. Cid *et al.* (2014) and references therein address the role of these eruptive phenomena and the geoeffectiveness of these features in extreme geomagnetic storms.

In this paper we focus on the case of the emergence of photospheric magnetic fields (using spectropolarimetric data) along with some detail on the eruption itself.

2. Data

We have mainly used data from the Helioseismic and Magnetic Imager (HMI, Scherrer *et al.* 2008) on board the Solar Dynamics Observatory (SDO, Pesnell *et al.* 2012) in the form of HMI magnetograms and full Stokes images, from 2013, 29 Sept. This analysis was also completed with data from AIA/SDO (Lemen *et al.* 2012) 171, 1600 Å. Data from the LASCO C2 coronagraph (Brueckner *et al.* 1995) onboard SOHO were checked for the eruption as well.

3. Flux emergence

We observed an event of flux emergence underneath a filament using HMI data. We analysed the magnetic flux density from the line-of-sight (LOS) magnetograms. Fig. 1 shows the maximum and minimum of this quantity, from 00:00 UT to 23:00 UT on

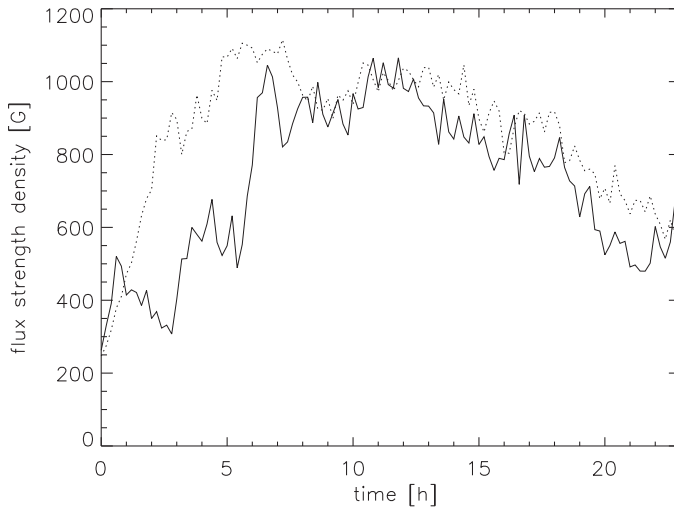


Figure 1. Maximum magnetic flux density from 00:00 UT to 23:00 UT. The solid line indicates the maximum (positive) magnetic flux density and the dashed line, the minimum (negative) magnetic flux density in absolute value.

Sept 29. These values are corrected for heliocentric angle projection (μ). Some network sub-structures exhibit longitudinal magnetic flux densities of the order of kilogauss (kG) during several hours.

Taking advantage of the full Stokes $[I, Q, U, V]$ imaging from HMI, we analysed the linear and circular polarization. We normalized the spectral profiles coarsely using the red-most wavelength point of Stokes I , and used the wavelength centering of this line (6173.34 Å, spacing 69 mÅ, Hoeksema *et al.* 2014). Fig. 2 shows the Stokes I (solid) and Stokes V (dashed) profiles corresponding to the pixels that display the largest negative and positive values in the magnetogram (note that the Stokes V profiles are clearly antisymmetric). To obtain the magnetic field strength density, we employed the weak-field approximation (Landi Degl’Innocenti & Landolfi 2004) with the HMI Stokes profiles. This leads also to kilogauss values in some pixels, in agreement to the HMI LOS-magnetograms.

Most likely, a mechanism of magnetic field intensification in the form of ‘convective collapse’ (Parker 1978, Spruit 1979) took place in this network patch, since it exhibits signals of small pore growth processes. For some case studies of this physical mechanism, see e.g., Vargas Domínguez *et al.* (2015) and references therein.

We also computed the linear and circular polarization from these Stokes profiles. Fig. 3 displays an image of the circular polarization at 10:00 UT, with some linear polarization contours overplotted. The background image corresponds to the maximum (in absolute value) of Stokes V (normalized to the continuum intensity) for each pixel, clipped at 0.03; the linear polarization contours mark the 0.0025 level with respect to the continuum intensity. The field of view (FOV) is $\sim 150'' \times 110''$.

4. Eruption

We also studied the evolution of different solar layers in order to know the correspondence of this flux emergence at different heights. We used AIA images from two different wavelengths, 1600 and 171 Å, which correspond to the high photosphere and corona, respectively. These are shown in Fig. 4. The field of view (FOV) is also $\sim 150'' \times 110''$.

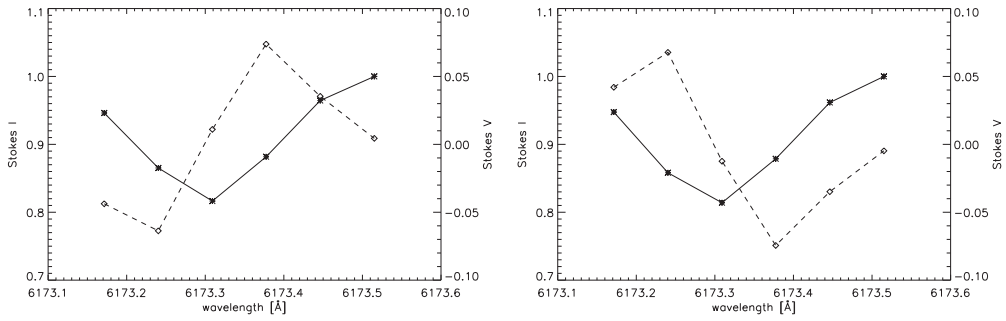


Figure 2. Stokes I (solid) and V (dashed, Y axis on the right) from the pixels that exhibit the largest extreme values in magnetic field strength (*left*: negative, *right*: positive).

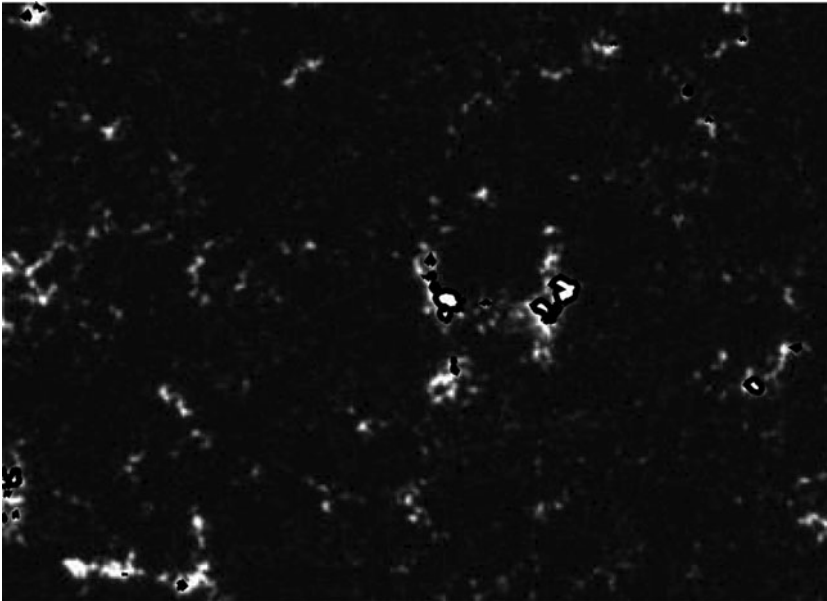


Figure 3. Background image: Absolute value of the maximum of Stokes V normalized to the continuum intensity. The image is clipped to 3% for clarity. The thick line contour represents the linear polarization normalized to the continuum intensity at 0.25% level.

The image in 1600 \AA (Fig. 4, left) shows a large network patch, the same as the one shown in the Stokes V image of Fig. 3, surrounded by other network areas. However, images in logarithmic scale in 171 \AA clearly display a brighter area, dipolar-shaped (Fig. 4, right). The filament is not seen in 171 \AA , since this channel is best for viewing the quiet corona, because it has a contribution from higher temperatures (O'Dwyer *et al.* 2010). The eruptive filament is clearly seen in high chromosphere - transition region wavelengths. We also looked for signatures of photospheric flux rope emergence in the data a few days before the eruption, following e.g. Kuckein *et al.* (2012), but unfortunately we could not detect it.

To have a wider FOV around the eruption, LASCO data were also employed. The LASCO C2 field of view ranges from 2 to 6 solar radii. Fig. 5 shows a LASCO C2 image of the eruption of this filament more than one hour after the eruption. It displays a twisted flux-rope structure in the solar north-west. The apex of the filament in this

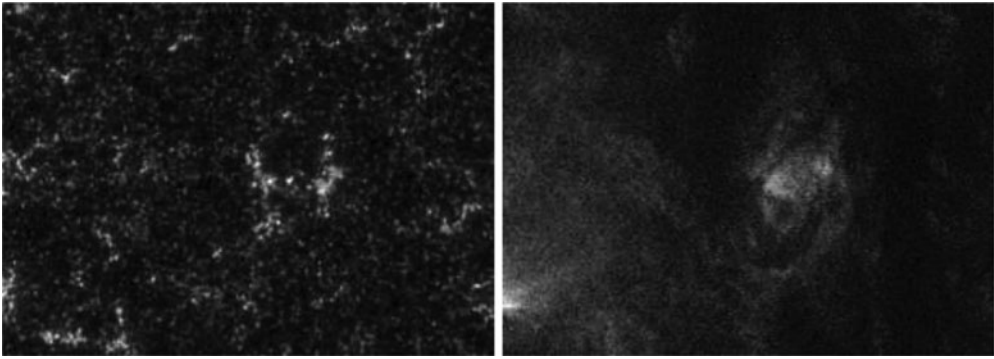


Figure 4. *Left:* Image in 1600 Å at 10:00 UT. *Right:* Image in 171 Å in logarithmic scale at the same moment.

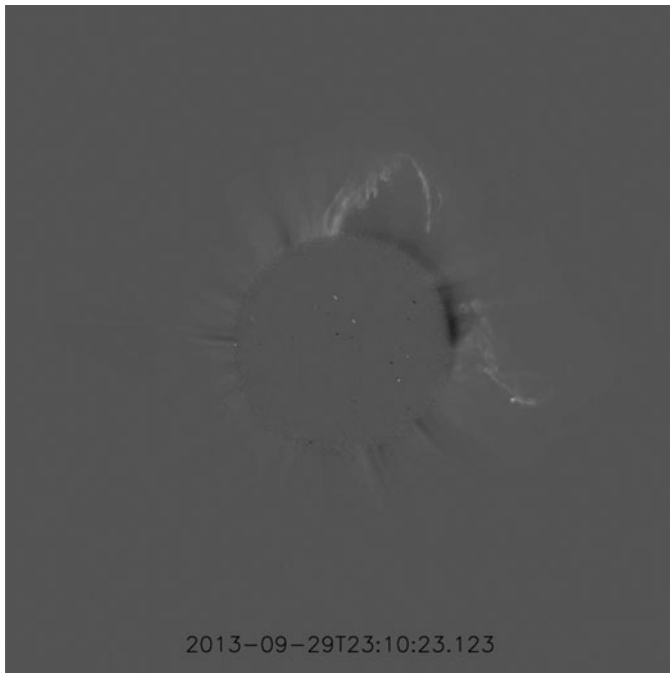


Figure 5. Image of the filament as observed by LASCO C2.

image is ~ 4 solar radii above the surface. The eruption speed of the filament is of the order of hundreds of km s^{-1} .

5. Final remarks

In this paper we analysed a flux emergence event related to a filament eruption, studying the longitudinal flux density, and the linear and circular polarization from HMI/SDO data. In addition, we measured the height and the shape of the filament in LASCO/SOHO images. We also investigated the emergence in different AIA wavelengths, namely, 171 and 1600 Å, which show an excellent correspondence in the high photosphere and the corona. A detailed study of this event will appear in a forthcoming paper.

Acknowledgements

We are very grateful to the HMI, AIA and LASCO teams for all valuable data used in this work. J. P. acknowledges funding from IAU to attend IAUS305 and UAH-travel grants. She also acknowledges project AYA2013-47735-P.

References

- Asai, A., K. Shibata, H. Hara, & N. V. Nitta, 2008, *ApJ* 673, 1188
- Brueckner, G. E., Howard, R. A., Koomen, M. J., Korendyke, C. M., Michels, D. J., Moses, J. D., Socker, D. G., Dere, K. P., Lamy, P. L., Llebaria, A., & 5 coauthors, 1995, *Solar Phys.* 162, 357
- Centeno, R., Socas-Navarro, H., Lites, B., Kubo, M., Frank, Z., Shine, R., Tarbell, T., Title, A., Ichimoto, K., Tsuneta, S., & 4 coauthors, 2007, *ApJ* 666, L137
- Centeno, R., 2012, *ApJ* 749, 72
- Cheung, M. C. M., Schüssler, M., Tarbell, T. D., & Title, A. M., 2008, *ApJ* 687, 1373
- Cheung, M. C. M., Rempel, M., Title, A. M., & Schüssler, M., 2010, *ApJ* 720, 233
- Cheung, M. C. M. & Isobe H., 2014, *Living Rev. Solar Phys.* 11, 3
- Cid, C., Palacios, J., Saiz, E., Guerrero, A., & Cerrato, Y., 2014, *JSWSC* 4, A28
- De Pontieu, B., 2002, *ApJ* 569, 474
- Gömöry, P., Beck, C., Balthasar, H., Rybák, J., Kucera, A., Koza, J., & Wóhrl, H., 2010, *A&A* 511, A14
- Guglielmino, S. L., Martínez Pillet, V., Bonet, J. A., del Toro Iniesta, J. C., Bellot Rubio, L. R., Solanki, S. K., Schmidt, W., Gandorfer, A., Barthol, P., & Knöölker, M., 2012, *ApJ* 745, 160
- Guglielmino, S. L., Martínez Pillet, V., Ruiz Cobo, B., del Toro Iniesta, J. C., Bellot Rubio, L. R., Solanki, S. K., & Sunrise/IMaX Team, 2013, *MemSAI* 84, 355
- Hagenaar, H. J., 2001, *ApJ* 555, 448
- Hoeksema, J. T., Liu, Y., Hayashi, K., *et al.*, 2014, *Solar Phys.* 289, 3483
- Krivova, N. A., Balmaceda, L., & Solanki, S. K., 2007, *A&A* 467, 335
- Kuckein, C., Martínez Pillet, V., & Centeno, R., 2012, *A&A* 539, A131
- Landi Degl'Innocenti, L. & Landolfi, M., 2004, *ASSL* vol. 307, Kluwer Academic Publishers
- Lemen, J. R., Title, A. M., Akin, D. J., Boerner, P.F., Chou, C., Drake, J.F., Duncan, D.W., Edwards, C.G., Friedlaender, F.M., Heyman, G.F., and 37 coauthors 2012, *Solar Phys.* 275, 17
- Martínez González, M. J. & Bellot Rubio, L. R., 2009, *ApJ* 700, 1391
- Martínez González, M. J., Manso Sainz, R., Asensio Ramos, A., & Bellot Rubio, L. R., 2010, *ApJL* 714, L94
- Martínez Pillet, V., 2013, *Space Sci. Revs* 178, 141
- O'Dwyer, B., Del Zanna, G., Mason, H. E. *et al.*, 2010, *A&A* 521, A21
- Orozco Suárez, D., Bellot Rubio, L. R., del Toro Iniesta, J. C., & Tsuneta, S., 2008, *A&A* 481, L33
- Palacios, J., Blanco Rodríguez, J., Vargas Domínguez, S., Domingo, V., Martínez Pillet, V., Bonet, J.A., Bellot Rubio, L.R., Del Toro Iniesta, J.C., Solanki, S.K., Barthol, P., and 4 coauthors, 2012, *A&A* 537, A21
- Parker, E. N., 1978, *ApJ* 221, 368
- Pesnell, W. D., Thompson, B. J., & Chamberlin, P. C., 2012, *Solar Phys.* 275, 3
- Rempel, M. & Cheung, M. C. M., 2014, *ApJ* 785, 90
- Scherrer, P. H., Schou, J., Bush, R. I., Kosovichev, A.G., Bogart, R.S., Hoeksema, J.T., Liu, Y., Duvall, T.L., Zhao, J., Title, A.M., and 3 coauthors, 2012, *Solar Phys.* 275, 207
- Schmieder, B., Archontis, V., & Pariat, E., 2014, *Space Sci. Revs* 186, 227
- Spruit, H. C., 1979, *Solar Phys.* 61, 363
- Tortosa-Andreu, A., & Moreno-Inertis, F., 2009, *A&A* 507, 949
- Valori, G., Green, L. M., Démoulin, V., Vargas Domínguez, S., van Driel-Gesztelyi, L., Wallace, A., Baker, D., & Fuhrmann, M., 2012, *Solar Phys.* 278, 73

- Vargas Domínguez, S., van Driel-Gesztelyi, L., & Bellot Rubio, L. R., 2012, *Solar Phys.* 278, 99
- Vargas Domínguez, S., Palacios, J., Balmaceda, L., Cabello, I., & Domingo, V., 2015, *Solar Phys.* 290, 301
- Wang, Y.-M. & Sheeley, Jr., N. R., 1999, *ApJL* 510, L157
- Zuccarello, F., Balmaceda, L., Cessateur, G., Cremades, H., Guglielmino, S.L., Lilensten, J., Dudok de Wit, T., Kretzschmar, M., Lopez, F.M., Mierla, M., and 8 coauthors, 2013, *JSWSC* 3, A18